# New Look on Fields and Energy Around Multiband Antennas: A Case Study Using Interdigital Capacitor–Loaded Monopoles

*Debdeep Sarkar and Yahia Antar*

*Abstract* – In this article, we critically examine the nonpropagating energy density distribution and propagating energy flow around multiband antennas in the frequency domain. Assuming a time-harmonic scenario, we first compute the time-averaged Poynting localized energy density and normalized energy-flow velocity in the near-field regime of arbitrary antennas at specific operating frequencies. As a specific example of compact multiband antenna, we consider one interdigital capacitor (IDC)–loaded planar monopole antenna and analyze it using the method-of-moments–based MATLAB Antenna Toolbox. First, we demonstrate the triple-band behavior and quasi-monopolar far-field gain characteristics at all three operating frequencies for these IDC-loaded monopoles. Next, we illustrate the two-dimensional maps of Poynting localized energy density and normalized energy-flow velocity in an observation plane near these IDC-loaded monopoles, which reveal interesting facts about the near-field propagating and nonpropagating energy dynamics for such multiband antennas.

## 1. Introduction

The subject of understanding the radiation mechanism of antennas along with the propagating energy flow and reactive (or "stored") energy dynamics around antennas has intrigued researchers over many decades [1–10]. In the present age of multiple-input multiple-output (MIMO) antennas in mobile handsets, massive MIMO base stations, and the Internet of things, compact multiband, multifunctional antenna systems are in great demand. Due to the close proximity of multiple antennas in such systems, significant interelement interaction occurs in the radiating and reactive near-field regions, implying that it is not prudent to limit the analysis of such antenna systems in the radiating far-field regime only [4]. Note that the traditional Q-factor approach and reactive energy evaluation for antenna near-field energy analysis definitely helps in understanding 1) antenna impedance matching characteristics and 2) the temporal evolution of total reactive energy in an observation volume around antennas [7]. However, the Q-factor does not quantify spatial distribution of reactive energy density around antennas, hence necessitating the need to look beyond the conventional realms of the antenna-Q factor and reactive energy [2–9]. Holistic space-time characterization of near-field reactive energy density around antennas can pave the way for mutual coupling reduction in multiantenna systems (MIMO and arrays) and for understanding the propagating/nonpropagating energy distribution around antennas installed on various platforms.

In the quest for understanding electromagnetic (EM) wave propagation and energy dynamics more closely in the near field of a radiating source, different researchers have explored concepts of electromagnetic inertia [2], energy flow velocity [3, 5], EM Lagrangian [6], and so on. Recently, a new approach has been introduced in [8, 9] that utilizes the finite-difference time-domain (FDTD) framework to compute space-time Poynting localized energy density around any antenna excited via an arbitrary temporal signal. In [10], electric and magnetic fields calculated via the FDTD technique and interpolation routines are used to compute EM Lagrangian density around antennas. It is shown that the evaluation of spatially averaged EM Lagrangian assists coupled ultrawide-band antenna system design [10].

However, in both [9] and [10], evaluation of Poynting localized energy and EM Lagrangian was done in the time domain (using the FDTD method), implying that the antenna excitation signal is a short-duration one, often Gaussian pulses. In order to analyze the near-field energy dynamics in a time-harmonic scenario, it is important to formalize concepts such as Poynting localized energy in the frequency domain. Furthermore, it is important to investigate the near-field "stored" energy density as well as energy flow around different operating frequencies of a compact multiband antenna, where the far-field radiation pattern might be very similar in all the working bands. As an example of such a compact multiband antenna, we use interdigital capacitor (IDC)–loaded planar monopoles. Such IDC-loaded monopoles have found use in pattern-diversity MIMO systems, circularly polarized antennas, and traveling wave active antennas for rocket communication [12–16]. The basic working principle of IDC loading essentially follows the resonant tank-circuit ("trap") loading principle [17].

With the motivation of closely investigating the radiated fields and near-field nonpropagating energy

Manuscript received 16 January 2022.

Debdeep Sarkar is with the Department of Electrical Communication Engineering, Indian Institute of Science, Bangalore, Bengaluru 560012, Karnataka, India; e-mail: debdeep@iisc.ac.in.

Yahia Antar is with the Department of Electrical and Computer Engineering, Royal Military College of Canada, PO Box 17000, Station Forces, Kingston K7K 7B4, Ontario, Canada; e-mail: antar-y@rmc.ca.

density around multiband antennas such as IDC-loaded monopoles, we presented some initial studies in [11]. The present article is a follow-up of [11], where we demonstrate the application of the MATLAB Antenna Toolbox in the computation of time-averaged Poynting localized energy density and normalized energy-flow velocity around generic antennas at any given frequency.

## 2. Spatial Maps of Poynting Localized Energy Density and Normalized Flow Velocity

We recall that the instantaneous Poynting localized energy density $\tilde{w}_{\text{loc}} = \tilde{w}_{\text{loc}}(\mathbf{r}, t)$ at a point with position vector $\mathbf{r}$ and time instant $t$ can be expressed in terms of total energy density $\tilde{u} = \tilde{u}(\mathbf{r}, t)$ and local Poynting vector $\tilde{\mathbf{S}} = \tilde{\mathbf{S}}(\mathbf{r}, t)$ as [8, 9]

$$\tilde{w}_{\text{loc}} = \tilde{u} - \frac{|\tilde{\mathbf{S}}|}{v} \tag{1}$$

where

$$\tilde{u} = \frac{1}{2}\varepsilon\tilde{\mathbf{E}} \cdot \tilde{\mathbf{E}} + \frac{1}{2}\mu\tilde{\mathbf{H}} \cdot \tilde{\mathbf{H}} \text{ and } \tilde{\mathbf{S}} = \tilde{\mathbf{E}} \times \tilde{\mathbf{H}} \tag{2}$$

Here, $\tilde{\mathbf{E}} = \tilde{\mathbf{E}}(\mathbf{r}, t)$ and $\tilde{\mathbf{H}} = \tilde{\mathbf{H}}(\mathbf{r}, t)$ represent the instantaneous electric and magnetic field intensities at P, and $\varepsilon$ and $\mu$ stand for, respectively, the value of permittivity and permeability at that point. The velocity of the EM wave is $v = 1/\sqrt{\mu\varepsilon}$, assuming the medium under consideration to be linear, isotropic, and homogeneous. For free space, $v$ simply reduces to $c = 1/\sqrt{\mu_0\varepsilon_0}$ (i.e., the speed of light).

In [8] and [9], we deployed the FDTD method and field-interpolation techniques to obtain $\tilde{\mathbf{E}}$ and $\tilde{\mathbf{H}}$ in the near field of antennas for any temporal excitation (which could be short-duration Gaussian pulses). Using these $\tilde{\mathbf{E}}$ and $\tilde{\mathbf{H}}$, one can obtain the spatiotemporal distribution of $\tilde{w}_{\text{loc}}$ and consequently calculate time/space-averaged quantities [8, 9]. In this article, we extend this time-domain approach introduced in [8, 9] for frequency-domain solvers such as the method-of-moments (MoM)–based MATLAB Antenna Toolbox. In such frequency domain solvers, one obtains a near-zone electric and magnetic field (in phasor form) around antennas having specific excitation amplitude and phase, considering the time-harmonic scenario (i.e., implicit $e^{j\omega t}$ time dependence). Note that the instantaneous field values $\tilde{\mathbf{E}}(\mathbf{r}, t)$ and $\tilde{\mathbf{H}}(\mathbf{r}, t)$ can be expressed in terms of phasors $\mathbf{E} = \mathbf{E}(\mathbf{r})$ and $\mathbf{H} = \mathbf{H}(\mathbf{r})$ as follows:

$$\tilde{\mathbf{E}} = \text{Re}\left[\mathbf{E}e^{j\omega t}\right] = \frac{1}{2}\mathbf{E}e^{j\omega t} + \frac{1}{2}\mathbf{E}^* e^{-j\omega t} \tag{3}$$

$$\tilde{\mathbf{H}} = \text{Re}\left[\mathbf{H}e^{j\omega t}\right] = \frac{1}{2}\mathbf{H}e^{j\omega t} + \frac{1}{2}\mathbf{H}^* e^{-j\omega t} \tag{4}$$

Previously, we used instantaneous $\tilde{w}_{\text{loc}}$ expression in terms of $\tilde{\mathbf{E}}$ and $\tilde{\mathbf{H}}$ and applied it in time-domain simulation paradigm. In the present scenario, we intend to obtain the expression for Poynting localized energy density $w_{\text{loc}} = w_{\text{loc}}(\mathbf{r})$ in terms of $\mathbf{E}$ and $\mathbf{H}$, which can be suitable for application in frequency-domain solvers.

With this objective, we recall the expressions for time-averaged total EM energy density $u_{\text{av}} = u_{\text{av}}(\mathbf{r})$ and time-averaged Poynting vector $\mathbf{S}_{\text{av}} = \mathbf{S}_{\text{av}}(\mathbf{r})$ at a point (proof given in the appendix)

$$u_{\text{av}} = \frac{1}{4}\varepsilon\mathbf{E} \cdot \mathbf{E}^* + \frac{1}{4}\mu\mathbf{H} \cdot \mathbf{H}^* \tag{5}$$

$$\mathbf{S}_{\text{av}} = \frac{1}{2}\text{Re}[\mathbf{E} \times \mathbf{H}^*] \tag{6}$$

Using $u_{\text{av}}$ and $\mathbf{S}_{\text{av}}$, we can obtain the expression of time-averaged Poynting localized energy density $w_{\text{loc}}$ as

$$w_{\text{loc}} = u_{\text{av}} - \frac{|\mathbf{S}_{\text{av}}|}{v} \tag{7}$$

Note that $w_{\text{loc}}$ is *not equal to* a simple time-averaged value of $\tilde{w}_{\text{loc}}$. Additionally, inspired from [3] and [5], we utilize the concept of normalized time-averaged energy flow velocity $v_{\text{norm}} = v_{\text{norm}}(\mathbf{r})$ as follows:

$$v_{\text{norm}} = \frac{|\mathbf{S}_{\text{av}}|}{vu_{\text{av}}} = \frac{2\sqrt{\mu\varepsilon}|\mathbf{E} \times \mathbf{H}^*|}{\varepsilon\mathbf{E} \cdot \mathbf{E}^* + \mu\mathbf{H} \cdot \mathbf{H}^*} \tag{8}$$

Using any frequency-domain full-wave simulation tool, one can obtain $\mathbf{E}$ and $\mathbf{H}$ at a point $\mathbf{r}$ around any antenna for a specific frequency. After that, the spatial maps (variation with respect to given $\mathbf{r}$) of $w_{\text{loc}}$ and $v_{\text{norm}}$ in the antenna near-field regime can be computed via (7) and (8). It can be shown that in the far-field regime (free space with $\varepsilon = \varepsilon_0$ and $\mu = \mu_0$), $w_{\text{loc}} \to 0$ and $v_{\text{norm}} \to 1$. In the subsequent section, we critically examine the spatial distribution of $w_{\text{loc}}$ and $v_{\text{norm}}$ around a representative compact multiband antenna (i.e., IDC-loaded monopole).

## 3. Case Study: Near Field Analysis of Triple-Band IDC-Loaded Monopoles

Figure 1 shows the schematic diagram of a single-port planar monopole of length $L_M$ and width $W_M$ mounted on a ground plane of area $L_g \times W_g$. An IDC structure of length $L_{idc}$ and finger width $w$ is etched out from the radiating arm of the monopole (Figure 1). Note that in this article, we perform mainly a conceptual analysis, so we consider monopole and ground made of a perfect electric conductor (PEC). But practically, planar monopoles with such IDC loading will be realized on a dielectric substrate, providing the much-needed mechanical stability (refer to [13] and [14] for more details on practical fabricated prototypes of IDC-loaded monopoles).

Figure 2 shows that without IDC loading, the original planar monopole of length $L_m$ and width $W_m$ of Figure 1 has the fundamental impedance matching point at 3.65 GHz. The $|S_{11}| \leq -10$ dB IBW (impedance bandwidth) in the lower band is 22.8% GHz. Note that

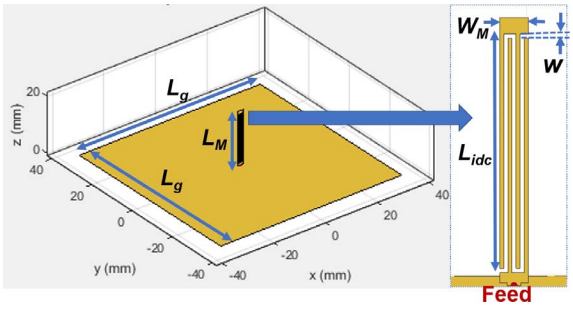


Figure 1. Schematic diagram of IDC-loaded planar monopole antenna on PEC ground plane. Dimensions (mm): $L_g = 70$, $L_M = 19$, $L_{idc} = 16.8$, $W_M = 2.1$, and $w = 0.3$.

$L_m = 0.23\lambda_1$ at $f_1 = 3.65$ GHz ($\lambda_1 = c/f_1$), confirming that the unloaded antenna operates in its fundamental quarter-wavelength monopole operating mode ($L_m \approx \lambda/4$). After the IDC loading as shown in Figure 1, the monopole exhibits triple-band characteristics with impedance matching points at 3.54 GHz, 3.98 GHz, and 4.83 GHz, respectively (Figure 2), with respective IBWs of 6.41%, 11.45%, and 1.65%. Similar triple-band response in an IDC-loaded monopole was depicted in [14].

Note that we have chosen values of $L_M$, $W_M$, $L_{idc}$, and $w$, the same as the CPW-fed monopole in [14]. The main two differences in the IDC-loaded monopole of Figure 1 with that of [14] are 1) the absence of dielectric substrate and 2) the presence of nonplanar ground plane. However, this does not affect the basic working principle of the IDC-loaded monopole. In fact, one can see that the presence of the dielectric substrate having relative permittivity $\varepsilon_r$ changes the effective dielectric constant around the monopole radiating arm, thereby effectively reducing all the operating frequencies by an approximate factor of $\sqrt{(\varepsilon_r + 1)/2}$. These multiple working frequencies (and corresponding IBWs) in the IDC-loaded monopole can be tailored by varying $L_{idc}$ [13, 14]. Figure 3 depicts the parametric variation of $|S_{11}|$-versus-frequency plots for different $L_{idc}$ values, highlighting the continuous tuning of the three bands by changing the length of IDC.

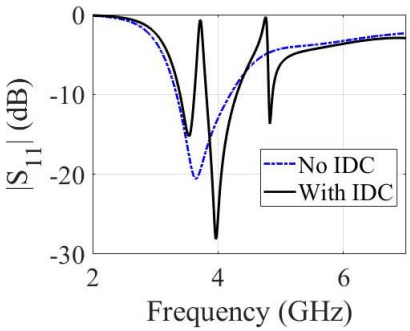


Figure 2. Frequency variation of $|S_{11}|$ for the monopole configuration of Figure 1 with and without IDC.

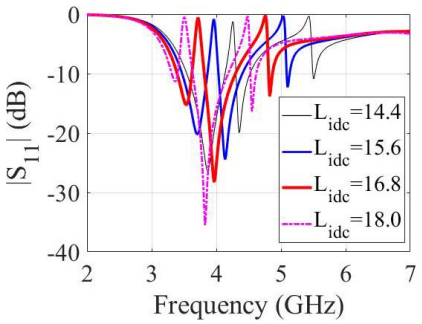


Figure 3. Parametric studies on frequency variation of $|S_{11}|$ (dB) for different values of $L_{idc}$ (in mm).

Figure 4 illustrates the simulated three-dimensional radiation patterns of the IDC-loaded monopole at 3.54 GHz, 3.98 GHz, and 4.83 GHz. The peak gains observed at these three frequencies are observed to be 3.45 dBi, 3.9 dBi, and 3.71 dBi, respectively, which are very close to the original unloaded monopole gain of 3.44 dBi at 3.65 GHz. Additionally, two-dimensional cuts of the radiation patterns in Figure 4 also confirm the quasi-monopolar characteristics of the IDC-loaded monopole at all three frequencies (azimuthal symmetry and null along the monopole axis).

Next, we apply (7) and (8) to find the distribution of normalized $w_{\text{loc}}$ and $v_{\text{norm}}$ along an observation region $x = 1$ mm away from the IDC-loaded monopole (see Figure 1), parallel to the $yz$-plane. The values of **E**

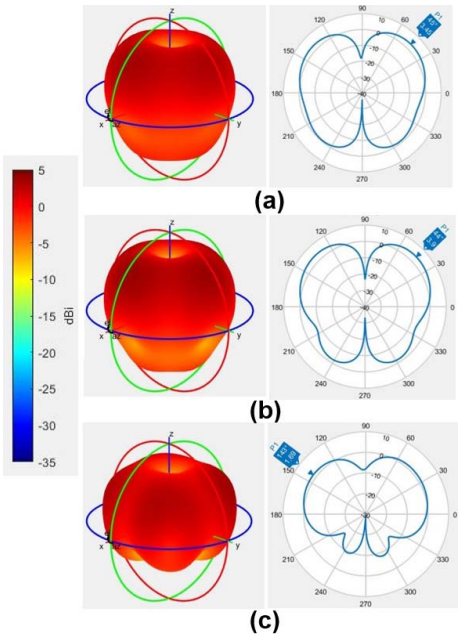


Figure 4. Simulated three-dimensional radiation patterns along with two-dimensional pattern cuts about elevation plane ($\phi = az = 0°$) for the planar monopole of Figure 1 (with IDC) at (a) 3.54 GHz, (b) 3.98 GHz, and (c) 4.83 GHz. Note that the two-dimensional pattern cuts are with respect to elevation angle $el$ and $el = 90°$, equivalent to $\theta = 0°$.

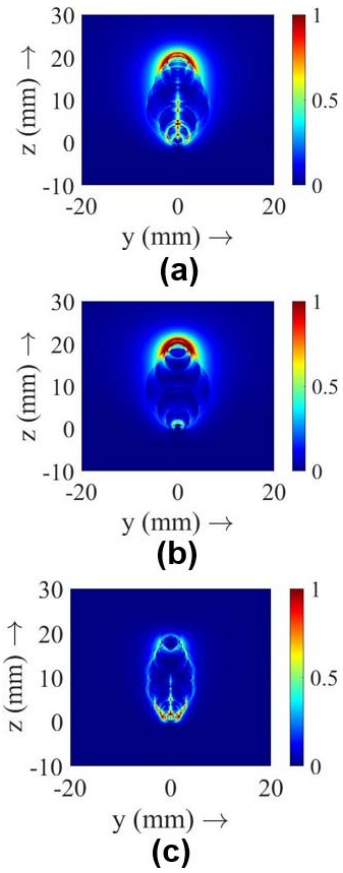


Figure 5. Spatial maps of normalized $w_{\text{loc}}$ about the observation plane $x = 1$ mm for the IDC-loaded monopole of Figure 1 at (a) 3.54 GHz, (b) 3.98 GHz, and (c) 4.83 GHz.

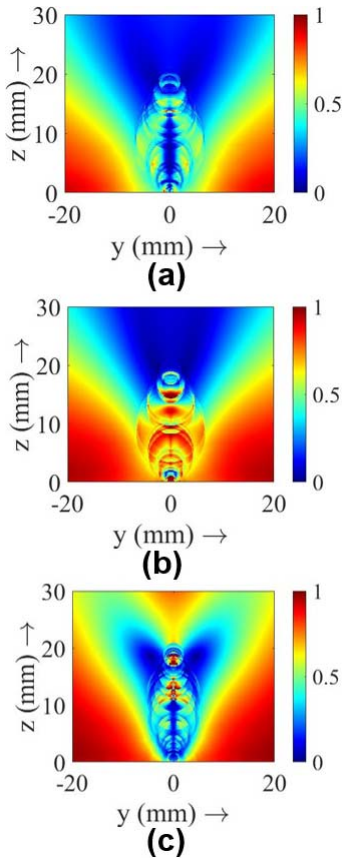


Figure 6. Spatial maps of $v_{\text{norm}}$ about the observation plane $x = 1$ mm for the IDC-loaded monopole of Figure 1 at (a) 3.54 GHz, (b) 3.98 GHz, and (c) 4.83 GHz.

and **H** at each of these spatial points on the observation region are obtained via the "EHFields" function of the MoM-based MATLAB Antenna Toolbox for the three working frequencies of the IDC-loaded monopole of Figure 1. Note that while $0 \leq v_{\text{norm}} \leq 1$ is inherently satisfied, the value of $w_{\text{loc}}$ is normalized with respect to its maximum value on the observation region so that it can be plotted in the range of 0 to 1.

Around the tip of the IDC-loaded monopole, a high value of normalized $w_{\text{loc}}$ at 3.54 GHz and 3.98 GHz can be observed; however, at 4.83 GHz, the intensity is much less (Figure 5). Figure 6 further demonstrates that the $v_{\text{norm}}$ reduces in close proximity of the radiating monopole arm. As one moves away from the monopole, one can observe $v_{\text{norm}} \to 1$ along the direction where far-field radiation dominates, which is expected.

Now the IDC-loaded monopole has far-field radiation null along $\theta = 0°$ for all the three frequencies, implying very low far-field energy flow in that direction (Figure 4). Interestingly, we have $v_{\text{norm}} \to 0$ near the monopole tip at 3.54 GHz and 3.98 GHz, but a high value of $v_{\text{norm}}$ is observed in that region at 4.83 GHz. This implies the potential of energy exchange along a spatial region in the antenna near field, where the traditional far-field energy flow is not possible. Clearly, the near-field propagating and nonpropagating energy dynamics around such compact resonator-loaded multiband antennas can vary, depending on the operating frequency.

## 4. Conclusion

In this article, we present a technique to obtain spatial plots of $w_{\text{loc}}$ and $v_{\text{norm}}$ around antennas at different operating frequencies, using the near-zone electric and magnetic field values computed via frequency-domain full-wave solvers (e.g., MoM-based MATLAB Antenna Toolbox). An example of IDC-loaded monopole is considered that provides triple-band response with monopolar radiation characteristics. Based on the results, it is evident that $w_{\text{loc}}$ and $v_{\text{norm}}$ are potentially useful for design of mutually coupled multiband antennas for antenna arrays and MIMO systems, as they uncover important information about energy dynamics around antennas in the reactive and radiating near-field regime.

## Appendix

Using (3) and (4) in (2), one obtains

$$\tilde{u} = \frac{1}{8}\varepsilon\left[(\mathbf{E}\cdot\mathbf{E})e^{2j\omega t} + 2(\mathbf{E}\cdot\mathbf{E}^*) + (\mathbf{E}^*\cdot\mathbf{E}^*)e^{-2j\omega t}\right] + \frac{1}{8}\mu\left[(\mathbf{H}\cdot\mathbf{H})e^{2j\omega t} + 2(\mathbf{H}\cdot\mathbf{H}^*) + (\mathbf{H}^*\cdot\mathbf{H}^*)e^{-2j\omega t}\right] \tag{9}$$

$$\begin{aligned}\tilde{\mathbf{S}} &= \tilde{\mathbf{E}}\times\tilde{\mathbf{H}} \\ &= \frac{1}{4}[(\mathbf{E}\times\mathbf{H})e^{2j\omega t} + (\mathbf{E}\times\mathbf{H}^*) + (\mathbf{E}^*\times\mathbf{H}) \\ &\quad + (\mathbf{E}^*\times\mathbf{H}^*)e^{-2j\omega t}] \\ &= \frac{1}{2}\mathrm{Re}\left[(\mathbf{E}\times\mathbf{H})e^{2j\omega t}\right] + \frac{1}{2}\mathrm{Re}[\mathbf{E}\times\mathbf{H}^*]\end{aligned} \tag{10}$$

The quantities $u_{av}$ and $\mathbf{S}_{av}$ are obtained, respectively, from $\tilde{u}$ and $\tilde{\mathbf{S}}$ by temporal averaging over the time period $T = 2\pi/\omega$. Therefore, the terms having $e^{2j\omega t}$ in $\tilde{u}$ and $\tilde{\mathbf{S}}$ do not contribute in $u_{av}$ and $\mathbf{S}_{av}$, and we obtain the expressions of (5) and (6).

## 5. References


1. H. G. Schantz, "Electromagnetic Energy Around Hertzian Dipoles," *IEEE Antennas and Propagation Magazine*, **43**, 2, April 2001, pp. 50-62.
2. G. Kaiser, "Electromagnetic Inertia, Reactive Energy and Energy Flow Velocity," *Journal of Physics A: Mathematical and Theoretical*, **44**, 34, August 2011, p. 345206.
3. C. A. Valagiannopoulos and A. Alu, "The Role of Reactive Energy in the Radiation by a Dipole Antenna," *IEEE Transactions on Antennas and Propagation*, **63**, 8, 2015, pp. 3736-3741.
4. S. Mikki and Y. M. M. Antar, *New Foundations for Applied Electromagnetics: Spatial Structures of Electromagnetic Field*, Norwood, MA, Artech House, 2016.
5. P. Saari, O. Rebane, and I. Besieris, "Energy-Flow Velocities of Non-Diffracting Localized Waves," *Physical Review A*, **100**, 2019, pp. 1-10.
6. H. G. Schantz, "Energy Velocity and Reactive Fields," *Philosophical Transactions of the Royal Society A*, **376**, 2018, p. 20170453.
7. D. Sarkar, S. Mikki, K. V. Srivastava, and Y. Antar, "Dynamics of Antenna Reactive Energy Using Time Domain IDM Method," *IEEE Transactions on Antennas and Propagation*, **67**, 2, 2019, pp. 1084-1093.
8. D. Sarkar, S. Mikki, and Y. Antar, "Poynting Localized Energy: Method and Applications to Gain Enhancement in Coupled Antenna Systems," *IEEE Transactions on Antennas and Propagation*, **68**, 5, 2020, pp. 3978-3988.
9. D. Sarkar, S. Mikki, and Y. Antar, "Representation of Electromagnetic Energy Around Antennas: Current Research and Future Directions," *IEEE Antennas and Propagation Magazine*, **63**, 5, 2021, pp. 61-71.
10. D. Sarkar and Y. Antar, "FDTD Computation of Space/Time Integrated Electromagnetic Lagrangian: New Insights Into Design of Mutually Coupled Antennas," *IEEE Journal on Multiscale and Multiphysics Computational Techniques*, **7**, 2022, pp. 16-22.
11. D. Sarkar and Y. Antar, "Analysis of Mutual Coupling and Energy Exchange Between Inter-Digital Capacitor Loaded Monopoles Using MoM and FDTD," URSI General Assembly (GASS), Rome, Italy, August 28–September 4, 2021.
12. J. Liu and W. Yin, "A Compact Interdigital Capacitor-Inserted Multiband Antenna for Wireless Communication Applications," *IEEE Antennas and Wireless Propagation Letters*, **9**, 2010, pp. 922-925.
13. A. Singh, D. Sarkar, K. Saurav, S. V. Reddy, and K. V. Srivastava, "A Via-Less Planar Quad-Band Monopole Antenna Employing Complementary Split Ring Resonator and Interdigital Capacitor," Proceedings of European Conference on Antennas and Propagation (EuCAP 2014), The Hague, Netherlands, April 6–11, 2014, pp. 1193-1196.
14. D. Sarkar, A. Singh, K. Saurav, and K. V. Srivastava, "Four Element Quad-Band Multiple-Input-Multiple-Output Antenna Employing Split Ring Resonator and Interdigital Capacitor," *IET Microwaves, Antenna and Propagation*, **9**, 13, 2015, pp. 1453-1460.
15. A. Singh, D. Sarkar, K. Saurav, and K. V. Srivastava, "Triple Band Circularly Polarized Printed Crossed Dipole Antenna Employing Interdigital Capacitors," IEEE UP Section Conference on Electrical Computer and Electronics (UPCON), Allahabad, India, December 4–6, 2015, doi: 10.1109/UPCON.2015.7456690.
16. C. E. Santosa and A. Munir, "Interdigital Capacitor Structure-Based Conformal Traveling Wave Active Antenna for Experimental Rocket Communication," Proceedings of International Conference on Quality in Research (QiR), Lombok, Indonesia, August 10–13, 2015, pp. 133-136.
17. D. Smith, "The Trap-Loaded Cylindrical Antenna," *IEEE Transactions on Antennas and Propagation*, **23**, 1, 1975, pp. 20-27.